In Situ Polymerized Interface Modulation Drives Spark Plasma Sintered Garnet Electrolyte-based Solid-State Lithium Metal Batteries

Asish Kumar Das[1,*] and Sunil Kumar[1,*]

[1] *Indian Institute of Technology Indore, Simrol, Indore, Madhya Pradesh, 453552, India*

*Corresponding author: phd2201105011@iiti.ac.in

*Corresponding author: sunil@iiti.ac.in

Abstract

Garnet-type solid electrolytes offer high ionic conductivity to be employed in solid-state lithium metal batteries. However, sluggish lithium-ion kinetics at the electrolyte-electrode interface hinder their application in full cells. Herein, we report the fabrication of a dense cubic-phase $Li_{6.5}La_3Zr_{1.5}Nb_{0.5}O_{12}$ (LLZNO) garnet solid electrolyte using the spark plasma sintering technique, with a conductivity of ~ 2.82×10^{-4} S cm^{-1} at room temperature. A free-radical-initiated in situ polymerization strategy using poly(ethylene glycol) dimethacrylate and tetraethylene glycol dimethyl ether was employed to establish intimate electrode-electrolyte interfacial contact. Consequently, the resulting polymer interlayer facilitates uniform lithium plating/stripping in lithium symmetric cells and provides lithium-ion conduit channels at the electrolyte-cathode interface in full cells. $LiFePO_4$ full cells delivered a high specific capacity (100 mAh g^{-1}) and exceptional cycling stability (90% capacity retention after 500 cycles) at 1C (30 °C).

Keywords: Solid electrolyte, spark plasma sintering, garnet, in situ polymerization, ionic conductivity

The global shift toward electrification and the integration of renewable energy requires safe, high-energy-density storage technologies. Lithium-ion batteries (LIBs) currently dominate the market but are approaching their theoretical limits in energy density. They pose a serious safety threat caused by thermal runaway due to flammable organic liquid in electric vehicles and portable daily-use electronic gadgets [1]. Lithium metal is the ideal anode material offering ultrahigh theoretical specific capacity (3860 mAh g^{-1}) and the lowest redox potential (–3.04 V vs. SHE) [2]. However, lithium metal is electrochemically unstable in liquid electrolytes, causing dendritic growth, continuous electrolyte decomposition, and low Coulombic efficiency [3]. These issues lead to poor cycling stability and serious safety hazards, including short circuits and thermal runaway [4]. Solid-state lithium metal batteries (SSLBs) with solid electrolytes are emerging as the next-generation solution, offering high energy density and improved operational safety [5-7].

Among various solid electrolytes (sulfides, polymers, halides, and oxides), garnet-type Garnet-based ceramic electrolytes have high ionic conductivity, excellent thermal stability, low interfacial resistance with lithium metal, and compatibility with high-voltage cathode materials [8-12]. However, fabrication of highly dense garnet pellets with minimal grain-boundary resistance is critical for achieving high ionic conductivity [13, 14]. Conventional sintering methods require long processing times (often 6-36 hours) at elevated temperatures (1100-1200 °C), leading to high lithium volatilization, secondary phase formation, and poor densification [15]. Spark plasma sintering (SPS) has emerged as a powerful alternative in the ceramics field for densifying in a shorter duration [16]. SPS applies direct current-mediated joule heating and uniaxial pressure simultaneously, enabling rapid heating rates (up to 1000 °C/min) and shorter dwell times (typically 5-30 minutes) [17-19]. This significantly reduces lithium volatilization and helps in obtaining highly dense pellets with a relative density >95% [20, 21].

However, the rigid nature of garnet electrolytes results in poor physical contact with electrodes, limiting lithium-ion transport at the electrodes' interfaces. Different interfacial engineering approaches, such as applying thin metallic buffer layers (such as Al, Sb, or Ag) and introducing polymer interphases, have been employed to mitigate this problem [14, 22, 23]. In-situ polymerization has recently gained attention for its ability to generate conformal, ionically conductive, and chemically stable interphases directly at the electrode-electrolyte interface [24].

This work demonstrates the fabrication of dense cubic-phase $Li_{6.5}La_3Zr_{1.5}Nb_{0.5}O_{12}$ (LLZNO) garnet pellets via SPS with high ionic conductivity. A free radical-mediated in-situ polymerization of poly(ethylene glycol) dimethacrylate (PEGDMA)-tetraethylene

glycol dimethyl ether (TEGDME) was employed to modulate the electrodes' interfaces of garnet electrolytes. This enables the formation of a stable solid electrolyte interphase (SEI) at the anode, while simultaneously providing lithium-ion conduction channels at the cathode interface. This strategy can pave the way for safe, high-energy-density solid-state lithium metal batteries.

The calcined (950 °C-6 h) powder's XRD pattern at room temperature is presented in Figure 1(a), along with the Rietveld refinement profile [25]. The refinement confirmed the cubic phase (space group: $Ia\bar{3}d$) with a lattice parameter of 12.9895(9) Å and volume of 2191.7(5) $Å^3$, and the lattice parameter value is in accordance with the reported literature [14]. Both Li sites (24d tetrahedral and the 96h octahedral) accommodate random lithium-ion distribution in the cubic garnet phase. Random lithium distribution facilitated by 0.4-0.5 lithium vacancy in the $Li_7La_3Zr_2O_{12}$ formula unit reduces Li-Li repulsion and stabilizes the cubic phase in lithium-stuffed garnet electrolytes ($Li_7La_3Zr_2O_{12}$) [26]. The 25% Zr^{4+} substitution by Nb^{5+} in $Li_7La_3Zr_2O_{12}$ creates 0.5 Li vacancy per formula unit, sufficient to prevent cubic-to-tetragonal phase transformation at room temperature. The partial vacancy at the distorted octahedral 96h site is critical for easier Li^+ transport through the crystal structure. Bond valence site energy (BVSE) calculations for Li^+ conduction pathways in LLZNO were performed using softBV software developed by Adams' group [27, 28]. The Vesta file generated from the software corresponding to the LLZNO CIF file was employed in visualizing the Li^+ conduction paths in the LLZNO electrolyte crystal structure, and it clearly indicated that Li^+ conducts via both 24d and 96h sites in the crystal (Figure 1(b)) [29].

The morphology and elemental distribution of SPS-sintered LLZNO pellet (1000 °C, ~25 MPa) were examined using a scanning electron microscope (SEM) and electron dispersive spectroscopy elemental mappings. The SEM image (Figure 1(c)) reveals a highly dense microstructure with no porosity, indicating effective densification during the SPS process, whereas Figure 1(d) indicates the uniform elemental distribution. It corroborates the relative density of ~98% calculated for the sintered pellet. The pellet's dimensions and the crystal density value from XRD results were used during the relative density calculation. Such dense and well-sintered microstructures are expected to reduce grain boundary resistance and boost the overall ionic conductivity of the ceramics-based solid electrolyte.

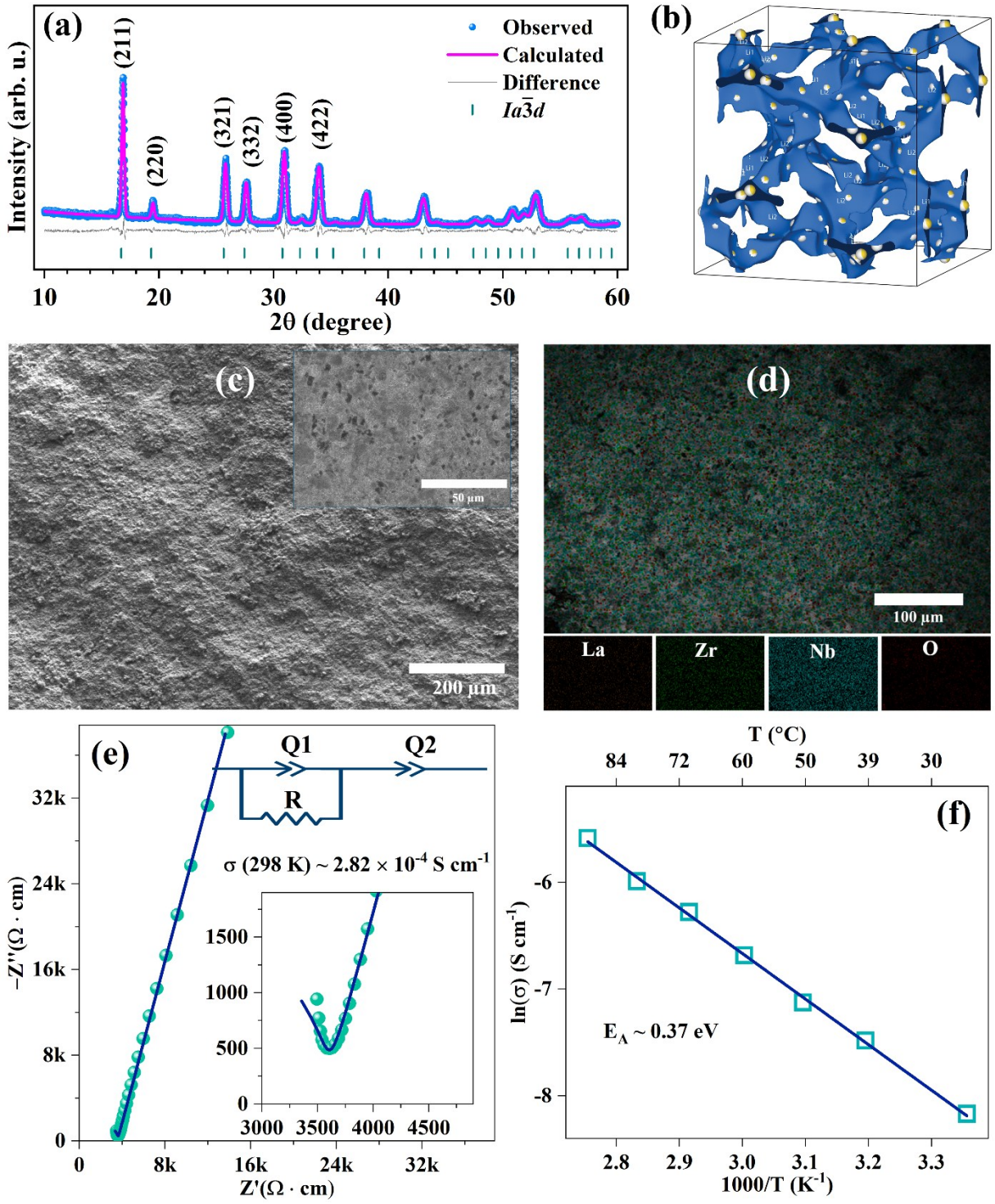

Figure 1:(a) Rietveld refinement of the room-temperature XRD pattern of $Li_{6.5}La_3Zr_{1.5}Nb_{0.5}O_{12}$. (b) Lithium ion migration pathway in the cubic $Li_{6.5}La_3Zr_{1.5}Nb_{0.5}O_{12}$ crystal structure. (c) Scanning electron microscopy image of a broken piece of SPS-sintered $Li_{6.5}La_3Zr_{1.5}Nb_{0.5}O_{12}$ solid electrolyte (inset shows image at higher magnification). (d) Electron dispersive spectroscopy elemental mappings of SPS-sintered $Li_{6.5}La_3Zr_{1.5}Nb_{0.5}O_{12}$ solid electrolyte. (e) Room temperature Nyquist plot of SPS-sintered $Li_{6.5}La_3Zr_{1.5}Nb_{0.5}O_{12}$ solid electrolyte (inset shows the equivalent circuit used for fitting). (f) Linear fitting of Arrhenius plot of conductivity values of SPS-sintered $Li_{6.5}La_3Zr_{1.5}Nb_{0.5}O_{12}$ solid electrolyte obtained at various temperatures.

The ionic conductivity of the LLZNO pellet was evaluated using electrochemical impedance spectroscopy (EIS), and the room temperature impedance data are presented in Figure 1(e). The Nyquist plot exhibited a small semicircular arc in the high-frequency region, corresponding to the combined bulk and grain boundary contributions, followed by a long linear tail in the low-frequency region with a slope >1, attributed to ion-blocking electrode/ion-conducting electrolyte interface polarization. The experimental data were fitted using an equivalent circuit model comprising two constant phase elements (Q1 and Q2) and one resistive component (R), as shown in the Figure 1(e) inset. The parallel combination of R and Q1 presents the ionic conduction in the solid electrolyte, whereas Q2 denotes the ion-blocking nature of the silver electrode. The resistance extracted from the fitted data and the pellet's geometric dimensions (l: thickness and A: area) were used to calculate the ionic conductivity (σ) via Ohm's law (σ = l/R×A). The SPS-sintered LLZNO pellet exhibited a conductivity of ~ 2.82×10^{-4} S cm^{-1} at room temperature (298 K), demonstrating competitive performance among garnet-type solid electrolytes. Temperature-dependent complex impedance spectroscopy measurements were performed in a temperature range of 40-90 °C, and the calculated conductivity values were used to obtain the activation energy, as shown in Figure 1(f), based on the Arrhenius equation (Eq. 1):

$$\sigma = \sigma_0 e^{\left(\frac{-E_a}{k_B T}\right)} \quad (1)$$

where σ represents the conductivity, σ_0 is the pre-exponential factor, E_a is the activation energy for lithium-ion migration, k_B is the Boltzmann constant, and T is the absolute temperature. A linear regression of the Arrhenius plot yielded an activation energy of ~0.37 eV, indicating a low energy barrier for lithium-ion transport through the garnet-type crystal structure. These results establish the LLZNO pellet as a viable solid electrolyte, enabling subsequent interfacial engineering and full cell integration.

The electrochemical performance of Li | LLZNO | Li symmetric cells incorporating the in-situ polymerized interlayer was systematically evaluated to assess interfacial stability and lithium plating/stripping behavior. Figure S1 presents FTIR-ATR spectra of the PEGDMA-TEGDME-Salt electrolyte before and after polymerization occurred. Before polymerization, the strong band at ~1716 cm^{-1} is assigned to the C=O stretching vibration, while the band at ~1638 cm^{-1} is due to the C=C stretching vibration in uncrosslinked PEGDMA [30]. The diminished peak at ~ 1638 cm^{-1} after polymerization confirms the cleavage of the C=C bond in the PEGDMA network, confirming the polymerization process. In the C=O band, the increased intensity indicates the crosslinking of PEGDMA, while a shift in the wavenumber is associated with the change in coordination following polymerization.

To assess the effects of the interlayer at the lithium metal interface, EIS data were recorded without and with the interlayer, as presented in Figure S2. The cell without polymer interlayer exhibited a total cell resistance of ~5000 Ω, while the introduction of the interlayer resulted in a significant reduction in total cell resistance of ~ 510 Ω. These results confirm that the interlayer plays a crucial role in enhancing interfacial compatibility and reducing charge-transfer resistance. Figure 2(a) shows lithium plating-stripping tests at progressively increasing current densities to determine operational limits. At lower current densities, the cell maintained a stable overpotential, suggesting uniform lithium deposition and stripping. Higher current densities caused increased polarization and sloped voltage profiles, reflecting greater ion transport resistance and potentially non-uniform lithium deposition. The cell maintained its electrical integrity even at 2 mA cm^{-2} (overpotential value > 1.5 V), which is beyond practical operational voltage limits.

To further assess the long-term cycling durability of the LLZNO electrolyte, galvanostatic charge-discharge cycling was performed for 450 cycles at a moderate current density of 0.2 mA cm^{-2}, as shown in Figure 2(b). Notably, the cell demonstrated highly stable cycling with negligible polarization growth and no evidence of either soft (noisy overpotential curves) or hard short-circuiting (fully flat overpotential curves) throughout the testing period. The nearly invariant overpotential across cycles and minimal drift indicate uniform Li plating/stripping and the presence of a stable Li-electrolyte interphase. Further, the Nyquist plots of Li|Li cells at 0 h and after 450 h of cycling at 0.2 mA/cm^2, shown in Figure S3, confirm only slight changes in impedance. The in-situ polymerization strategy not only provides facile lithium-ion kinetics at the LLZNO-electrode interface but also accommodates the interfacial stress from volume changes during cycling.

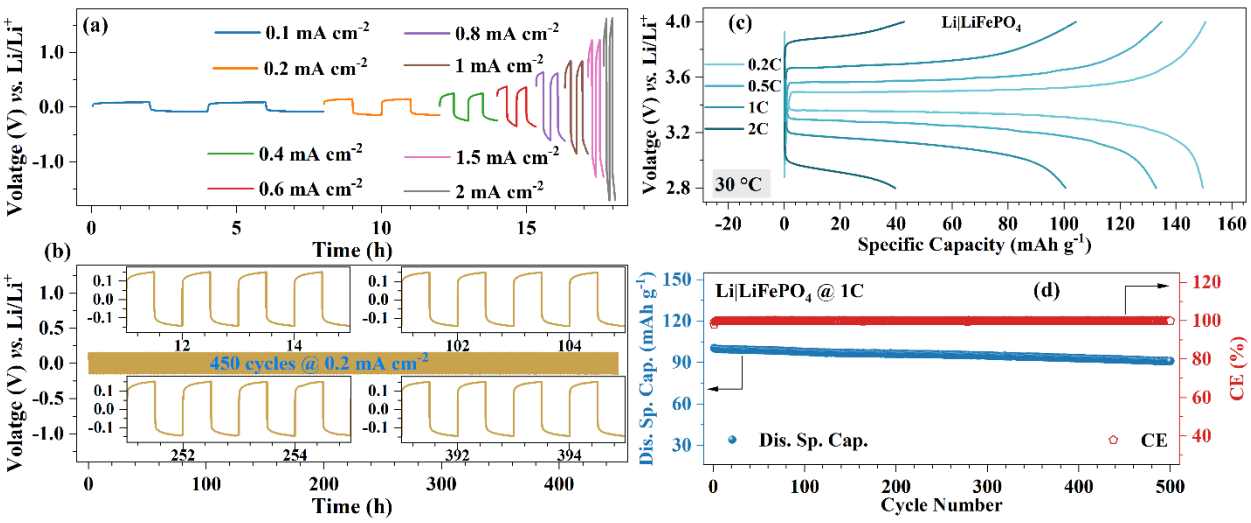

Figure 2:(a) The lithium plating-stripping overpotential curves at different current densities. (b) The lithium plating/stripping behavior at 0.2 mA cm^{-2} for 450 h. (c) Galvanostatic charge-discharge specific capacity-voltage curves at 30 °C. (d) Long-term cyclability of Li | $LiFePO_4$ cell at 1C (30 °C).

To evaluate the solid electrolyte's viability in full cells, galvanostatic charge-discharge measurements in Li | LiFePO4 cells were conducted at progressively increasing current densities at 30 °C, as presented in Figure 2(c). The cell exhibited stable voltage profiles across all applied C-rates, maintaining the characteristic flat discharge plateau of the LFP cathode, indicative of the reversible two-phase transition between $FePO_4$ and $LiFePO_4$ during lithiation and delithiation processes. At a low current density of 0.2C, the cathode delivered a high specific discharge capacity of approximately 149 mAh g^{-1}, accompanied by a narrow voltage hysteresis between charge and discharge plateaus. This low polarization reflects good lithium-ion pathways at the electrolyte-cathode interface.

With increasing current densities, the discharge capacity gradually decreased to ~132 mAh g^{-1} at 0.5C, 100 mAh g^{-1} at 1C, and 40 mAh g^{-1} at 2C, with a concomitant increase in charge voltage plateau and decrease in discharge voltage plateau.

As illustrated in Figure 2(d), the solid-state cell exhibited exceptional cycling stability, retaining approximately ~97% of its initial discharge capacity after 100 cycles at 1C with a coulombic efficiency of ~99.9%. This indicates negligible parasitic side reactions and intimate interfacial contact between electrode particles and the solid electrolyte, facilitated by the in-situ polymerization. Further galvanostatic charge-discharge experiments were performed on $LiFePO_4$ full cells across a temperature range of 20–60 °C at various current densities, and the capacity-voltage profiles are presented in Figure 3.

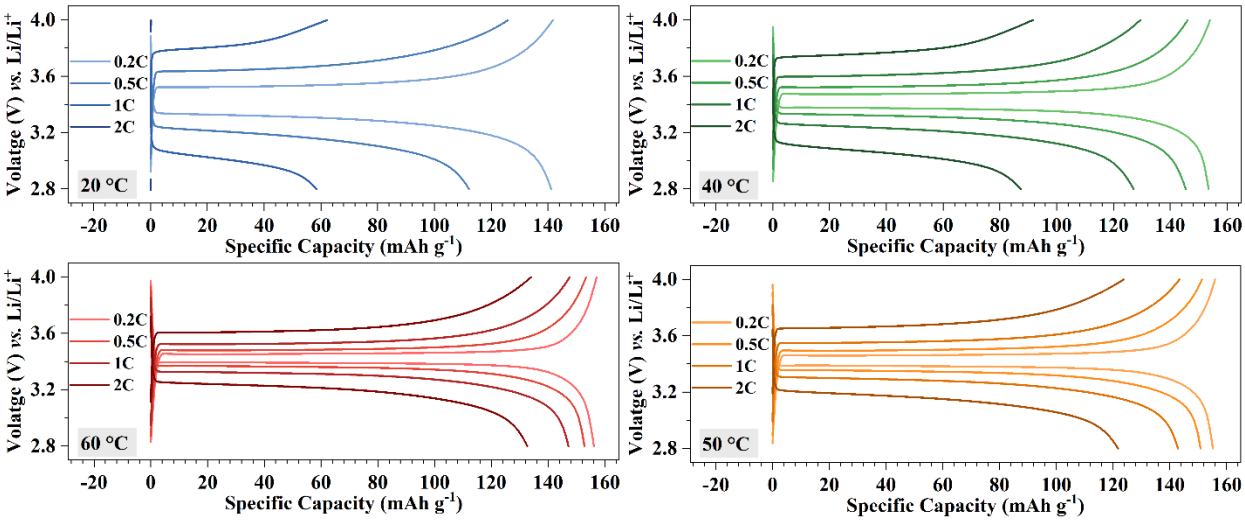

Figure 3: Galvanostatic charge-discharge specific capacity-voltage curves at different temperatures.

At 20 °C, the full cell delivered a discharge capacity of ~140 mAh g^{-1} (0.2C), ~111 mAh g^{-1} (0.5C), and ~58 mAh g^{-1} (1C) in the 2.8-4.0 V range. No capacity was observed at 2C due to the higher polarization. However, elevating the operating temperature to 40 °C, 50 °C, and 60 °C resulted in substantial capacity improvements at all tested C-rates. Notably, at 60 °C, the discharge capacity at 0.2 C increased significantly to ~ 156 mAh g^{-1}, approaching the practical capacity limit of $LiFePO_4$. The effect of temperature on the electrochemical performance is drastic at higher C-rates. At a current density equivalent to 2C, the cell delivered almost zero capacity at 20 °C, compared to ~132 mAh g^{-1} at 60 °C. This enhancement is attributed to reduced polarization potential and accelerated lithium-ion diffusion kinetics at elevated temperatures, which facilitate more efficient charge transfer and mass transport processes. Figure 4 presents temperature-dependent dQ/dV versus V curves at different C-rates. At 0.2C, as the temperature decreased from 60°C to 20°C, the separation between the lithiation and delithiation redox peaks increased gradually, along with an increase in peak broadening. In contrast, at 2C, there is a drastic change in the difference in values of redox peaks with decreased temperature. To assess the impact of temperature on full cell impedance, EIS measurements at different temperatures were performed, and the results are shown in Figure S4. With the increase in temperature from 20 °C to 60 °C, there is a significant decrease in the cell's total resistance. It corroborates the better high C-rate performance at higher temperatures. These findings demonstrate that operation at moderately elevated temperatures improves the electrochemical performance of LLZNO-based solid-state full cells. This underscores the potential of the engineered garnet electrolyte system for practical solid-state battery applications.

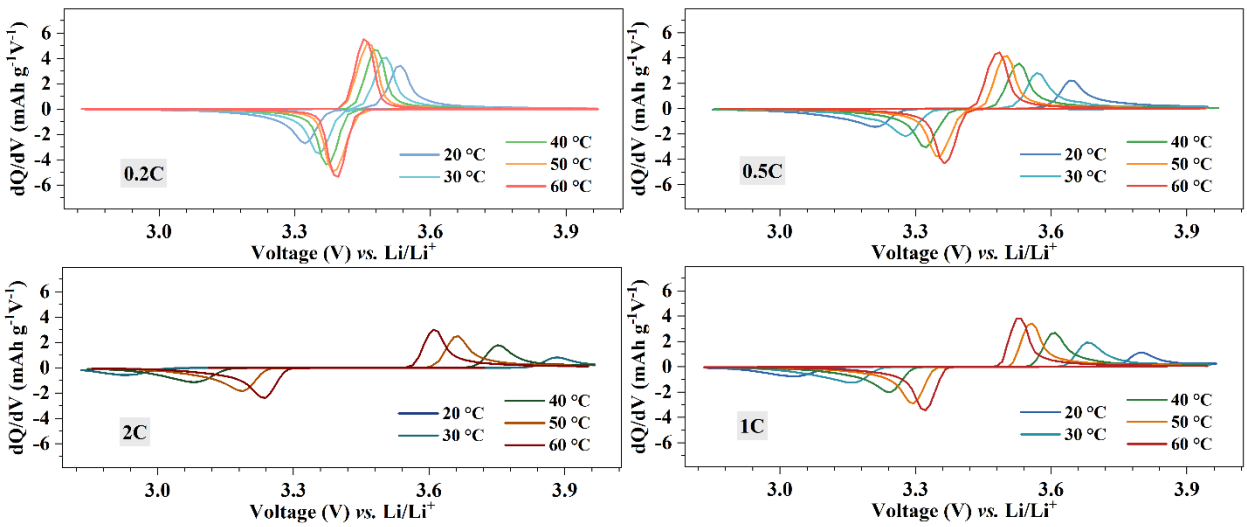

Figure 4: Temperature-dependent galvanostatic charge-discharge voltage-differential specific capacity curves at different C-rates.

In conclusion, LLZNO garnet solid electrolyte was successfully synthesized with a pure cubic phase (space group: $Ia\bar{3}d$). SPS technique was employed to obtain highly dense (~ 98% relative density) solid electrolyte pellets with conductivity of ~ 2.82 × 10^{-4} S cm^{-1} in minutes, as compared to hours required through the conventional sintering methods. A conformal polymer interlayer was applied directly on the LLZNO garnet electrolyte surface via in situ polymerization, establishing compliant mechanical contact with the lithium metal anode. Symmetric Li | LLZNO | Li cells cycled stably for over 450 h at 0.2 mA cm^{-2} with low overpotential, showing no dendrite formation, voltage fluctuations, or short-circuits. Stable performance demonstrates that the polymer interlayer effectively homogenizes lithium flux and accommodates interfacial stress. At 30 °C, $LiFePO_4$ full cells delivered 149 mAh g^{-1} at 0.2C and 40 mAh g^{-1} (2C). Long-term cycling at 1C showed 90% capacity retention after 500 cycles, with a coulombic efficiency of ~99.9%. At 60 °C, performance improved to 156 mAh g^{-1} (0.2C) and 132 mAh g^{-1} (2C) due to reduced polarization and enhanced ion transport kinetics. The SPS-sintered LLZNO coupled with in situ polymerization-driven facile electrode-electrolyte interface demonstrates practical viability for solid-state lithium metal batteries through its robust electrochemical performance.

Conflicts of Interest

There are no conflicts of interest to declare.

Data Availability Statement

The data that support the findings of this study are available from the corresponding authors upon reasonable request.

Credit author statement

Asish Kumar Das: Conceptualisation, Methodology, Investigation, Funding acquisition, Data curation, Formal analysis, Writing - Original Draft; **Sunil Kumar:** Funding acquisition, Supervision, Resources, Project administration, Validation, Writing - Review and Editing.

Supporting Information

Experimental details; FTIR Spectra of electrolyte before and after polymerization; EIS of symmetric cell with and without interlayer; EIS of symmetric cell with interlayer before and after lithium plating and stripping; EIS of full cells at different temperatures.

Acknowledgments

The author (AKD) thanks the Ministry of Education, Government of India, for the Prime Minister's Research Fellowship (PMRF) (PMRF ID - 2102737). The authors gratefully acknowledge the Ministry of Education (MoE), Government of India (Grant No. MoE-STARS/STARS-2/2023-0365). The financial support for SPS equipment provided by the Department of Science and Technology (DST), Government of India, through the FIST funding (SR/FST/ET-II/2021/778) is acknowledged. The authors acknowledge Professor Satyanarayan Patel (Energy Materials Research Lab, Department of Mechanical Engineering, Indian Institute of Technology Indore, India) for access to the impedance measurements facility and Professor Preeti A. Bhobe (Quantum Materials & Magnetism Lab, Department of Physics, Indian Institute of Technology Indore, India) for providing the Diamond Saw cutter facility

References

[1] K. Liu, Y. Liu, D. Lin, A. Pei, Y. Cui, Materials for lithium-ion battery safety, Sci. Adv., 4 (2018) eaas9820, DOI: https://doi.org/10.1126/sciadv.aas9820.

[2] P. Bonnick, J. Muldoon, The quest for the holy grail of solid-state lithium batteries, Energy Environ. Sci., 15 (2022) 1840-1860, DOI: https://doi.org/10.1039/D2EE00842D.

[3] C. Fang, J. Li, M. Zhang, Y. Zhang, F. Yang, J.Z. Lee, M.-H. Lee, J. Alvarado, M.A. Schroeder, Y. Yang, et al., Quantifying inactive lithium in lithium metal batteries, Nature, 572 (2019) 511-515, DOI: https://doi.org/10.1038/s41586-019-1481-z.

[4] K.L. Jungjohann, R.N. Gannon, S. Goriparti, S.J. Randolph, L.C. Merrill, D.C. Johnson, K.R. Zavadil, S.J. Harris, K.L. Harrison, Cryogenic Laser Ablation Reveals Short-Circuit Mechanism in Lithium Metal Batteries, ACS Energy Lett., 6 (2021) 2138-2144, DOI: https://doi.org/10.1021/acsenergylett.1c00509

[5] S. Puls, E. Nazmutdinova, F. Kalyk, H.M. Woolley, J.F. Thomsen, Z. Cheng, A. Fauchier-Magnan, A. Gautam, M. Gockeln, S.Y. Ham, et al., Benchmarking the reproducibility of all-solid-state battery cell performance, Nat. Energy, 9 (2024) 1310-1320, DOI: https://doi.org/10.1038/s41560-024-01634-3.

[6] J. Cao, J. Meng, H. Shen, X. Ye, H. Liu, C. Guo, J. Li, G. Zhang, W. Bao, F. Yu, Solid-state electrolytes for next-generation Batteries: Recent advances and interfacial challenges, J. Power Sources, 654 (2025) 237870, DOI: https://doi.org/10.1016/j.jpowsour.2025.237870.

[7] X. Wu, G. Ji, J. Wang, G. Zhou, Z. Liang, Toward Sustainable All Solid-State Li–Metal Batteries: Perspectives on Battery Technology and Recycling Processes, Adv. Mater., 35 (2023) 2301540, DOI: https://doi.org/10.1002/adma.202301540.

[8] A.K. Das, M. Badole, H.N. Vasavan, S. Saxena, P. Gami, S. Kumar, Highly conductive ceramic-in-polymer composite electrolyte enabling superior electrochemical performance for all-solid-state lithium batteries, Ceram. Int., 49 (2023) 29719-29728, DOI: https://doi.org/10.1016/j.ceramint.2023.06.214.

[9] A.K. Das, P. Gami, H.N. Vasavan, S. Saxena, N. Dagar, S. Deswal, P. Kumar, S. Kumar, Advancing High-Energy Solid-State Batteries with High-Entropy NASICON-type Solid Electrolytes, ACS Appl. Energy Mater., 7 (2024) 8301-8307, DOI: https://doi.org/10.1021/acsaem.4c02011.

[10] P. Gami, M. Badole, H.N. Vasavan, A.K. Das, S. Saxena, N. Dagar, V. Srihari, S. Kumar, NASICON-type medium entropy $Li_{1.5}Sn_{1.0}Al_{0.5}Zr_{0.5}(PO_4)_3$ electrolyte for solid state Li metal batteries, J. Power Sources, 618 (2024) 235214, DOI: https://doi.org/10.1016/j.jpowsour.2024.235214.

[11] R. Murugan, V. Thangadurai, W. Weppner, Fast Lithium Ion Conduction in Garnet-Type $Li_7La_3Zr_2O_{12}$, Angew. Chem. Int. Ed., 46 (2007) 7778, DOI: https://doi.org/10.1002/anie.200701144.

[12] X. Kong, R. Gu, Z. Jin, L. Zhang, C. Zhang, W. Xiang, C. Li, K. Zhu, Y. Xu, H. Huang, et al., Maximizing interface stability in all-solid-state lithium batteries through entropy stabilization and fast kinetics, Nat. Commun., 15 (2024) DOI: https://doi.org/10.1038/s41467-024-51123-0.

[13] Y. Kim, H. Jo, J.L. Allen, H. Choe, J. Wolfenstine, J. Sakamoto, The Effect of Relative Density on the Mechanical Properties of Hot-Pressed Cubic $Li_7La_3Zr_2O_{12}$, J. Am. Ceram. Soc., 99 (2016) 1367-1374, DOI: https://doi.org/10.1111/jace.14084.

[14] A.K. Das, S. Kumar, Compositionally Tuned High-Entropy Li-Garnet Electrolyte for Advanced Solid-State Batteries, Batter. Supercaps, 0 (2025) e202500358, DOI: https://doi.org/10.1002/batt.202500358.

[15] M. Fukuda, Y. Li, J. Wei, K. Harata, G. Luo, G.J. Snyder, Y.S. Sato, H. Kato, E.J. Cheng, High-Temperature Sintering of Garnet Solid Electrolyte $Li_7La_3Zr_2O_{12}$: A Comparative

Study of Induction Hot Pressing and Spark Plasma Sintering, Small, 21 (2025) e06257, DOI: https://doi.org/10.1002/smll.202506257.

[16] O. Guillon, J. Gonzalez-Julian, B. Dargatz, T. Kessel, G. Schierning, J. Räthel, M. Herrmann, Field-Assisted Sintering Technology/Spark Plasma Sintering: Mechanisms, Materials, and Technology Developments, Adv. Eng. Mater., 16 (2014) 830-849, DOI: https://doi.org/10.1002/adem.201300409.

[17] M. Ihrig, M. Finsterbusch, A.M. Laptev, C.-h. Tu, N.T.T. Tran, C.-a. Lin, L.-Y. Kuo, R. Ye, Y.J. Sohn, P. Kaghazchi, et al., Study of $LiCoO_2/Li_7La_3Zr_2O_{12}$:Ta Interface Degradation in All-Solid-State Lithium Batteries, ACS Appl. Mater. Interfaces, 14 (2022) 11288-11299, DOI: https://doi.org/10.1021/acsami.1c22246.

[18] H. Yamada, T. Ito, T. Nakamura, R. Bekarevich, K. Mitsuishi, S.P. Kammampata, V. Thangadurai, High Cathode Loading and Low-Temperature Operating Garnet-Based All-Solid-State Lithium Batteries – Material/Process/Architecture Optimization and Understanding of Cell Failure, Small, 19 (2023) 2301904, DOI: https://doi.org/10.1002/smll.202301904.

[19] M. Clausnitzer, M. Ihrig, L. Cressa, S. Hein, M. Finsterbusch, S. Eswara, L.-Y. Kuo, T. Danner, P. Kaghazchi, D. Fattakhova-Rohlfing, et al., Impact of degradation mechanisms at the cathode/electrolyte interface of garnet-based all-solid-state batteries, Energy Storage Mater., 67 (2024) 103262, DOI: https://doi.org/10.1016/j.ensm.2024.103262.

[20] S.-W. Baek, J.-M. Lee, T.Y. Kim, M.-S. Song, Y. Park, Garnet related lithium ion conductor processed by spark plasma sintering for all solid state batteries, J. Power Sources, 249 (2014) 197-206, DOI: https://doi.org/10.1016/j.jpowsour.2013.10.089.

[21] Y. Dabaki, M. Kassem, G. Delaizir, A. Sammoury, G. Leroy, C. Poupin, M. Bokova, E. Bychkov, The garnet Al-LLZO lithium-ion conductor processed by spark plasma sintering: Phase formation and ionic conductivity, Ceram. Int., 51 (2025) 18816-18826, DOI: https://doi.org/10.1016/j.ceramint.2025.02.061.

[22] J.-S. Kim, G. Yoon, S. Kim, S. Sugata, N. Yashiro, S. Suzuki, M.-J. Lee, R. Kim, M. Badding, Z. Song, et al., Surface engineering of inorganic solid-state electrolytes via interlayers strategy for developing long-cycling quasi-all-solid-state lithium batteries, Nat. Commun., 14 (2023) 782, DOI: https://doi.org/10.1038/s41467-023-36401-7.

[23] R. Dubey, J. Sastre, C. Cancellieri, F. Okur, A. Forster, L. Pompizii, A. Priebe, Y.E. Romanyuk, L.P.H. Jeurgens, M.V. Kovalenko, et al., Building a Better Li-Garnet Solid Electrolyte/Metallic Li Interface with Antimony, Adv. Energy Mater., 11 (2021) 2102086, DOI: https://doi.org/10.1002/aenm.202102086.

[24] A.K. Das, S. Kumar, In Situ Polymerization-Enabled Facile Electrode Interface in Solid-State Lithium–Metal Batteries, ACS Appl. Electron. Mater., 7 (2025) 9994-10000, DOI: https://doi.org/10.1021/acsaelm.5c01889.

[25] A. Coelho, TOPAS and TOPAS-Academic: an optimization program integrating computer algebra and crystallographic objects written in C++, J. Appl. Crystallogr., 51 (2018) 210, DOI: https://doi.org/10.1107/S1600576718000183.

[26] T. Thompson, J. Wolfenstine, J.L. Allen, M. Johannes, A. Huq, I.N. David, J. Sakamoto, Tetragonal vs. cubic phase stability in Al-free Ta doped $Li_7La_3Zr_2O_{12}$ (LLZO), J. Mater. Chem. A, 2 (2014) 13431, DOI: https://doi.org/10.1039/c4ta02099e.

[27] H. Chen, L.L. Wong, S. Adams, SoftBV - a software tool for screening the materials genome of inorganic fast ion conductors, Acta. Crystallogr. B., 75 (2019) 18, DOI: https://doi.org/10.1107/S2052520618015718.

[28] L.L. Wong, K.C. Phuah, R. Dai, H. Chen, W.S. Chew, S. Adams, Bond Valence Pathway Analyzer—An Automatic Rapid Screening Tool for Fast Ion Conductors within softBV, Chem. Mater., 33 (2021) 625, DOI: https://doi.org/10.1021/acs.chemmater.0c03893.

[29] K. Momma, F. Izumi, VESTA: a three-dimensional visualization system for electronic and structural analysis, J. Appl. Crystallogr., 41 (2008) 653, DOI: https://doi.org/10.1107/S0021889808012016.

[30] S. Choudhury, S. Stalin, D. Vu, A. Warren, Y. Deng, P. Biswal, L.A. Archer, Solid-state polymer electrolytes for high-performance lithium metal batteries, Nat. Commun., 10 (2019) 4398, DOI: https://doi.org/10.1038/s41467-019-12423-y.

[TOC Graphic]

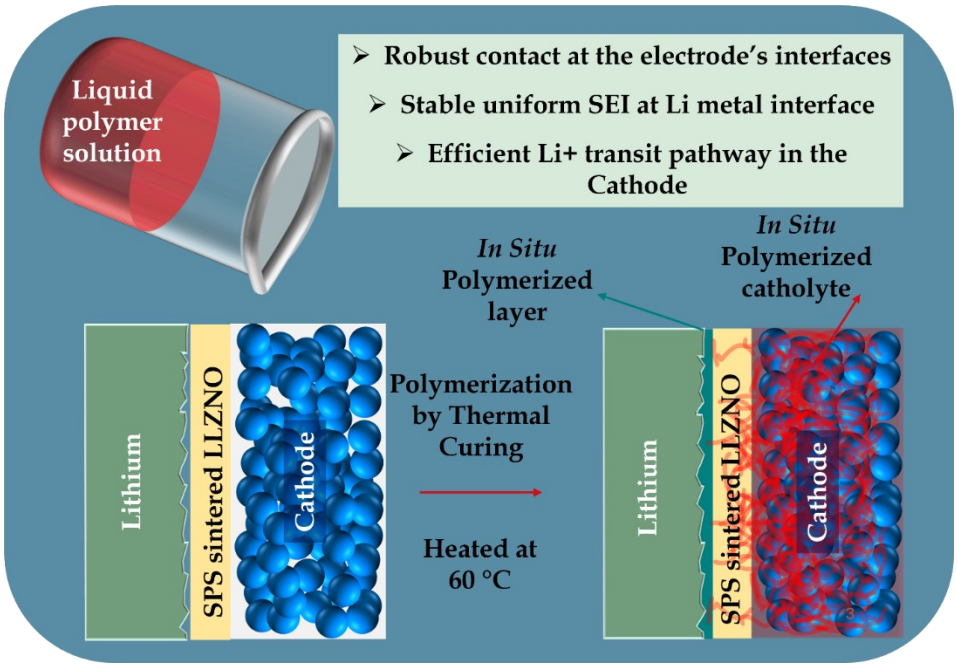

[Supporting Information]

In Situ Polymerized Interface Modulation Drives Spark Plasma Sintered Garnet Electrolyte-based Solid-State Lithium Metal Batteries

Asish Kumar Das[1,*] and Sunil Kumar[1,*]

[1] *Indian Institute of Technology Indore, Simrol, Indore, Madhya Pradesh, 453552, India*

*Corresponding author: phd2201105011@iiti.ac.in

*Corresponding author: sunil@iiti.ac.in

Experimental Section

Synthesis of LLZNO powder

To synthesize $Li_{6.5}La_3Zr_{1.5}Nb_{0.5}O_{12}$, calculated amounts of precursors LiOH, La_2O_3, Nb_2O_5, and ZrO_2 were hand-ground using a mortar, followed by ball-milling at 300 rpm for 12 h. The solvent used for mixing was ethanol. La_2O_3 was preheated at 900 °C for 12 h before use, and 20 wt.% extra LiOH was used. The mixed precursor slurry was dried and calcined at 950 °C (dwelling time: 6 h). The calcined powder was transferred to the Ar-filled MBraun Glovebox (H_2O < 0.1 ppm & O_2 < 0.1 ppm) for further characterization.

SPS Sintering of LLZNO

The calcined LLZNO powder was compacted into a 16-mm-diameter green pellet in a stainless-steel die set. Then, the green pellets were inserted into a graphite die for SPS sintering at 1000 °C with a constant dwelling time of 300 s and a constant force of 5 kN. The heating and cooling rates were controlled by an in-built pyrometer of the SPS machine above 300 °C. The heating rate was 600 °C/min (from 300 °C to the set sintering temperature), and the cooling rate was 25 °C/min until 600 °C, followed by 50 °C/min until 300 °C, and then normal cooling to 30 °C.

Relative Density Measurement

The Archimedes method was used to calculate the relative density of the sintered pellet using Xylene as the solvent. The formula used is as follows:

$$\rho_{\,pellet} = \frac{Weight\ in\ air}{Weight\ in\ air - Weight\ in\ xylene} \times \rho_{\,xylene}$$

Where, $\rho_{\,pellet}$ = density of pellet, $\rho_{\,xylene}$ = density of xylene.

Then the relative density of the pellet is ($\rho_{\,pellet}$ / $\rho_{\,theoritical}$) × 100, where $\rho_{\,theoritical}$ was determined from the unit cell mass and volume calculated from XRD data.

Preparation of polymer-salt solution for in situ polymerization

The solid polymer electrolyte was prepared via free radical polymerization. The components were mixed to achieve a poly(ethylene glycol) dimethacrylate (PEGDMA): tetraethylene glycol dimethyl ether (TEGDME) volume ratio of 3:6. 0.5 M LiTFSI and 0.5 M LiFSI were used to make the polymer lithium-ion conductive. For stable SEI formation at the lithium metal anode, $LiNO_3$ was added with a Li: EO molar ratio of 0.1. AIBN content (~ 1 wt.% relative to PEGDMA) was added to the solution mixture. The mixture was stirred at room temperature until all components were fully dissolved and a homogeneous solution was obtained.

Coin cell fabrication

The symmetric lithium cells, denoted as Li|LLZNO|Li, were assembled using lithium metal chips on either side of the pellet, and the above-mentioned polymer-salt solution was used to enhance the contact at the electrode-electrolyte interface. The fabricated CR2032 cells were heated at 60 °C for 12 h to initiate the polymerization before electrochemical testing.

Full cells: slurries (NMP solvent) of $LiFePO_4$ (LFP) cathodes (PVDF binder: electronically conducting Ketjen black: $LiFePO_4$ active material weight ratio ~ 10:10:80) were cast onto aluminum current collectors using an automatic doctor-blade machine and then transferred into a vacuum oven for drying. After drying, the punched circular cathodes (active material: 1-2 mg cm^{-2}) were transferred into an Ar-filled glovebox. During the full-cell fabrication, the aforementioned polymer-salt solution was used at both the Li-LLZNO and LFP-LLZNO interfaces. The whole configuration was crimped in a coin cell CR2032 using a hydraulic crimping machine inside the glovebox. Then, the cells were stored at 60 °C for 24 h to allow in situ polymerization to occur before electrochemical testing.

Characterization

The material characterization was conducted using various techniques. X-ray diffraction (XRD) analysis was performed on an Empyrean X-ray diffractometer equipped with Cu-Kα radiation (wavelength: 1.54 Å, current: 40 mA, voltage: 30 kV), covering a 2θ range of 10° to 60°. Crystallographic parameters were determined from the XRD data using Rietveld refinement with the TOPAS academic version 6 software [1]. FTIR-ATR data were collected in a Perkin-Elmer Spectrum IR (Model number: Spectrum 2). The microstructural features of the synthesized samples and elemental mapping were observed using a JEOL-7610+ field emission scanning electron microscope (FE-SEM). The complex impedance spectroscopy data were obtained with an NF (Model: ZM2376) LCR meter over the frequency range of 1 Hz to 1 MHz with a sinusoidal voltage amplitude of 100 mV on LLZNO solid electrolyte pellets (Ag electrodes painted on both sides of the

polished pellets). Constant-current charge-discharge measurements were performed on lithium symmetric and full cells using a Neware BTS4000-5V20mA battery tester.

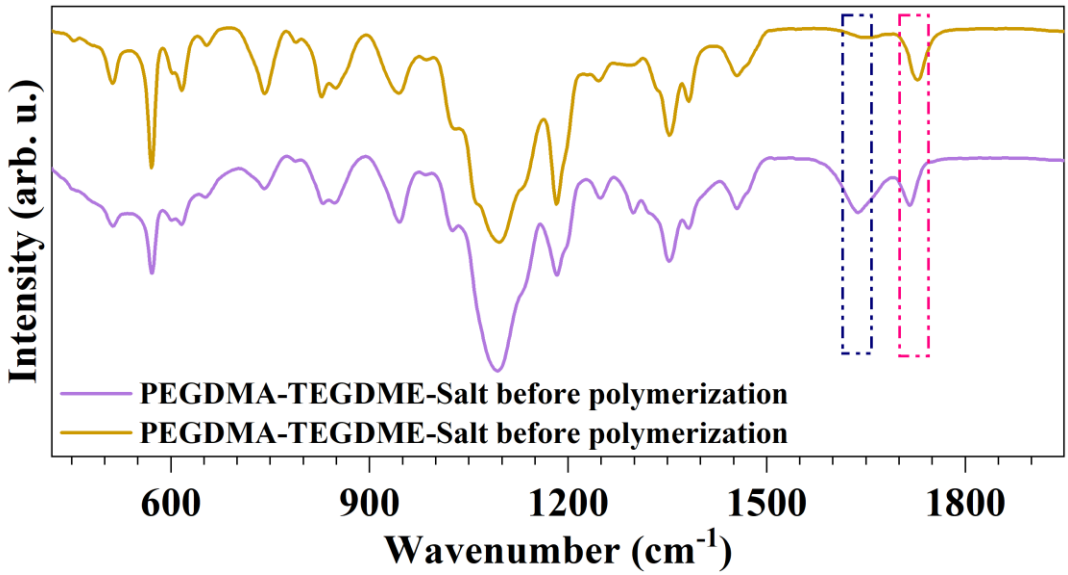

Figure S1: FTIR-ATR spectra of the PEGDMA-TEGDME-LiTFSi-LiFSI-$LiNO_3$-AIBN before and after polymerization.

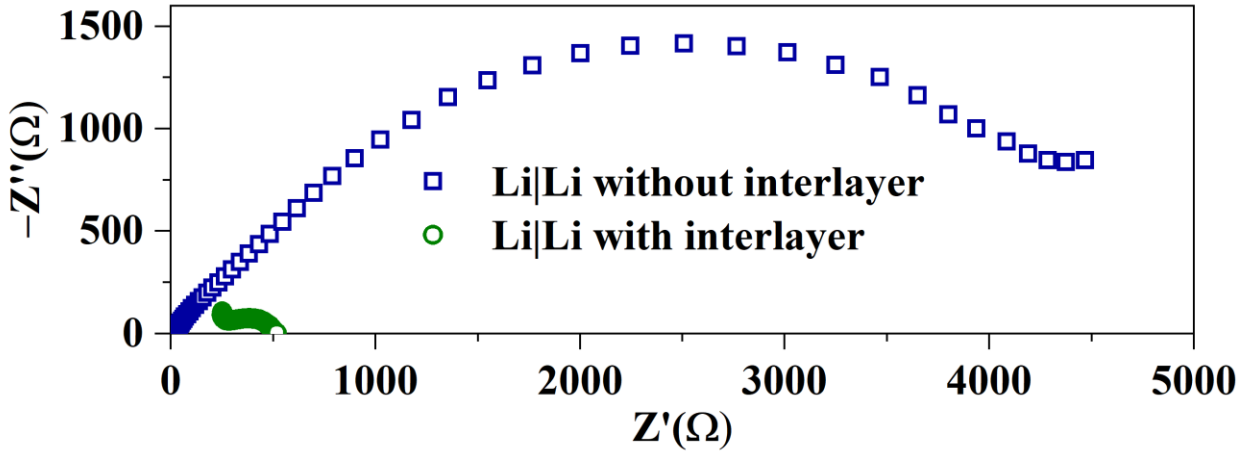

Figure S2: Room-temperature Nyquist plots of Li | Li symmetric cells without and with in situ polymerized interlayer.

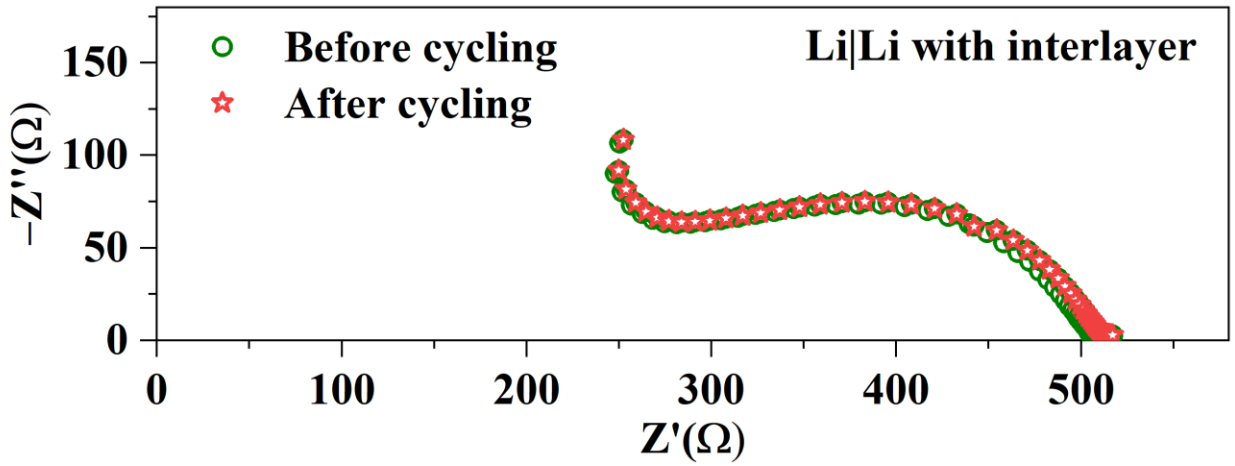

Figure S3: Room-temperature Nyquist plots of Li | Li symmetric cells before and after lithium plating-stripping for 450 cycles.

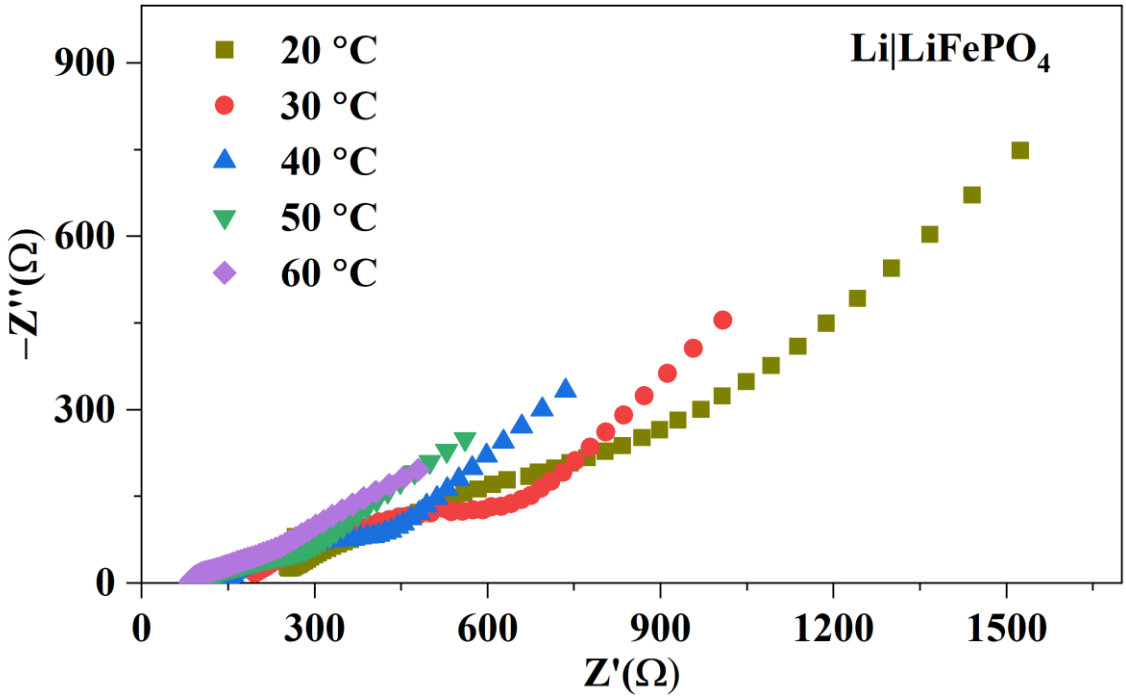

Figure S4: Room-temperature Nyquist plots of Li | $LiFePO_4$ full cells at different temperatures.

Reference

[1] A. Coelho, TOPAS and TOPAS-Academic: an optimization program integrating computer algebra and crystallographic objects written in C++, J. Appl. Crystallogr., 51 (2018) 210.